

The monoclinic crystal structure of α -RuCl₃ and the zigzag antiferromagnetic ground state

R. D. Johnson,^{1,2,*} S. C. Williams,¹ A. A. Haghighirad,¹ J. Singleton,³ V. Zapf,³
P. Manuel,² I. I. Mazin,⁴ Y. Li,⁵ H. O. Jeschke,⁵ R. Valentí,⁵ and R. Coldea¹

¹*Clarendon Laboratory, University of Oxford Physics Department,
Parks Road, Oxford, OX1 3PU, United Kingdom*

²*ISIS Facility, Rutherford Appleton Laboratory-STFC, Chilton, Didcot, OX11 0QX, United Kingdom*

³*National High Magnetic Field Laboratory MPA-NHMFL, TA-35,
MS-E536 Los Alamos National Laboratory, Los Alamos, NM 87545, USA*

⁴*Code 6393, Naval Research Laboratory, Washington, DC 20375, USA*

⁵*Institut für Theoretische Physik, Goethe-Universität Frankfurt, 60438 Frankfurt am Main, Germany*
(Dated: December 16, 2015)

The layered honeycomb magnet α -RuCl₃ has been proposed as a candidate to realize a Kitaev spin model with strongly frustrated, bond-dependent, anisotropic interactions between spin-orbit entangled $j_{\text{eff}} = 1/2$ Ru³⁺ magnetic moments. Here we report a detailed study of the three-dimensional crystal structure using x-ray diffraction on un-twinned crystals combined with structural relaxation calculations. We consider several models for the stacking of honeycomb layers and find evidence for a parent crystal structure with a monoclinic unit cell corresponding to a stacking of layers with a unidirectional in-plane offset, with occasional in-plane sliding stacking faults, in contrast with the currently-assumed trigonal 3-layer stacking periodicity. We report electronic band structure calculations for the monoclinic structure, which find support for the applicability of the $j_{\text{eff}} = 1/2$ picture once spin orbit coupling and electron correlations are included. Of the three nearest neighbour Ru-Ru bonds that comprise the honeycomb lattice, the monoclinic structure makes the bond parallel to the b -axis non-equivalent to the other two, and we propose that the resulting differences in the magnitude of the anisotropic exchange along these bonds could provide a natural mechanism to explain the previously reported spin gap in powder inelastic neutron scattering measurements, in contrast to spin models based on the three-fold symmetric trigonal structure, which predict a gapless spectrum within linear spin wave theory. Our susceptibility measurements on both powders and stacked crystals, as well as magnetic neutron powder diffraction show a single magnetic transition upon cooling below $T_N \approx 13$ K. The analysis of our neutron powder diffraction data provides evidence for zigzag magnetic order in the honeycomb layers with an antiferromagnetic stacking between layers. Magnetization measurements on stacked single crystals in pulsed field up to 60 T show a single transition around 8 T for in-plane fields followed by a gradual, asymptotic approach to magnetization saturation, as characteristic of strongly-anisotropic exchange interactions.

I. INTRODUCTION

There has been considerable recent interest in materials that realize strongly-anisotropic, bond-dependent interactions as the resulting frustration effects could potentially stabilize novel forms of cooperative magnetic order or a spin liquid state.¹ A canonical Hamiltonian is the Kitaev spin model on the honeycomb lattice,² where each bond carries an Ising interaction, but where the Ising axes are reciprocally orthogonal for the three bonds meeting at each lattice site, leading to an exotic quantum spin liquid state with fractional spin excitations. In a pioneering set of papers^{3,4} it was proposed that Kitaev physics may be realized in $\mathcal{A}_2\text{IrO}_3$ ($\mathcal{A} = \text{Na, Li}$) materials with a tri-coordinated, edge-sharing bonding geometry of IrO₆ octahedra. Here the combined effect of strong spin-orbit coupling at the Ir⁴⁺ 5d⁵ site and near-cubic crystal field of the O₆ octahedra stabilize $j_{\text{eff}} = 1/2$ Ir moments, and superexchange via two near 90° Ir-O-Ir paths is predicted to couple (to leading order) only the magnetic moment components normal to the plane of the Ir-O-Ir bond, with three such near-orthogonal planes meeting at each Ir site. Evidence for dominant Kitaev interactions in such mate-

rials has been observed in the structural polytypes β - and γ -Li₂IrO₃ where the Ir ions have the same local threefold coordination as in the planar honeycomb, but now form fully-connected three-dimensional networks, so-called hyperhoneycomb and striphoneycomb, respectively. In both structural polytypes complex counter-rotating and non-coplanar incommensurate magnetic orders have been observed,^{5,6} which cannot be reproduced by isotropic (Heisenberg) exchanges, but require the presence of dominant ferromagnetic Kitaev interactions⁷⁻⁹ supplemented by additional smaller interactions. In contrast, the layered honeycomb iridate Na₂IrO₃ shows a very different magnetic order, with spins arranged in zigzag ferromagnetic chains aligned antiferromagnetically,¹⁰⁻¹² believed to be stabilized by the competition between many interactions including a strong ferromagnetic Kitaev term and further neighbor interactions.¹³ In Na₂IrO₃ evidence for the presence of strong Kitaev interactions has been provided by measurements of the diffuse scattering at temperatures above the magnetic ordering transition temperature, which observed a locking of the polarization of spin fluctuations with the wavevector direction.¹⁴

α -RuCl₃ has been proposed¹⁵ as a candidate Kitaev

material in a $4d$ analogue of the layered honeycomb iridates. This might be surprising at first as the spin-orbit coupling is expected to be considerably weaker in Ru compared to Ir (due to the smaller atomic number), but it was argued^{15,16} that i) the crystal field of the Cl_6 octahedra may potentially be much closer to cubic in $\alpha\text{-RuCl}_3$ as layers are only very weakly bonded (by van der Waals interactions), in contrast to Na_2IrO_3 where the O_6 octahedra are strongly trigonally squashed due to the strong bonding to the adjacent hexagonal Na^+ layers, and ii) correlation effects in a narrow band could potentially enhance the effects of spin-orbit coupling.

The magnetic properties of $\alpha\text{-RuCl}_3$ are currently the subject of much experimental and theoretical investigation.^{15,17–23} Early studies have established the existence of two distinct structural polytypes: the α polytype with edge-sharing RuCl_6 octahedra forming stacked honeycomb layers with magnetic order below ≈ 14 K [Ref. 24], and the β polytype with face-sharing RuCl_6 octahedra arranged in chains, which shows no magnetic ordering down to the lowest temperatures measured.²⁵ However, detailed studies of the three-dimensional crystal structure of the layered (α) polytype have proved difficult because of the prevalence of diffuse scattering due to stacking faults,²⁶ an inevitable consequence of the weak bonding between adjacent honeycomb layers. A trigonal space group $P3_112$ with a 3-layer stacking periodicity is usually presupposed based on an early structural study,²⁷ although this structural model has been questioned by later studies.^{28–30} In particular, Ref. 29 reported a monoclinic $C2/m$ stacking of honeycomb layers for the related halide IrBr_3 (AlCl_3 structure type³¹) and proposed, by analogy, a similar structural framework for $\alpha\text{-RuCl}_3$, but no lattice parameters or any other structural details were provided. The difficulty in reliably solving the crystal structure stems from the fact that in principle several candidate stacking sequences of the honeycomb layers may be possible (monoclinic, trigonal, rhombohedral - to be discussed later) and it is experimentally rather challenging to reliably distinguish between them in the presence of stacking faults and/or when samples may contain multiple twins. Having a reliable determination of the full three-dimensional crystal structure is important for understanding the underlying electronic and magnetic properties, as electron hopping terms, and consequently magnetic interactions and anisotropies, appear to be quite sensitive to the stacking sequence of layers and to weak distortions inside each layer, as we will show later in Sec. V.

Previous studies on single crystals of $\alpha\text{-RuCl}_3$ have observed two anomalies near 8 and 14 K in both magnetic susceptibility and heat capacity^{17,19,20} (with the transition near 8 K attributed¹⁷ to the onset of zigzag magnetic order as in Na_2IrO_3), whereas studies on powder samples showed only one anomaly near $T_N \approx 13$ K [Refs. 24 and 25], raising the question of why the powders and single crystals show distinct behaviors. To date, the ground state magnetic structure is yet to be reported for sam-

ples that exhibit a single magnetic phase transition upon lowering temperature.

Here, we report comprehensive results and an extensive discussion of x-ray diffraction measurements on *untwinned* crystals of $\alpha\text{-RuCl}_3$ that display a single magnetic phase transition upon cooling to low temperatures, in agreement with powder samples. We find that the crystal structure is monoclinic, with space group $C2/m$. Features in the diffraction pattern necessitated by the assumed trigonal $P3_112$ model are clearly absent. The monoclinic structure of $\alpha\text{-RuCl}_3$ is found to be isostructural to the layered honeycomb materials Na_2IrO_3 [Ref. 11] and $\alpha\text{-Li}_2\text{IrO}_3$ [Ref. 32]. From neutron powder diffraction data, we present evidence of a magnetic propagation vector, $\mathbf{k}=(0,1,0.5)$, consistent with *zigzag* or *stripy* long-range magnetic ordering. We find that the calculated magnetic diffraction pattern expected for the stripy model is inconsistent with the experimental data and conclude that the zigzag model with antiferromagnetic stacking gives the best account of the true magnetic structure. Furthermore, we characterize the stability of the zigzag order in applied magnetic field and construct a magnetic phase diagram for field applied in the honeycomb layers. To complement the x-ray diffraction studies we report electronic band structure calculations to check the stability of the crystal structure and determine the resulting magnetic ground state of the Ru^{3+} ions.

The paper is organized as follows: Sec. II presents the methods employed. Single crystal diffraction results are given in Sec. III, with the space-group determination and stacking faults analysis presented in Sec. III A, the structural refinement discussed in Sec. III B, and comparison to other structural models drawn in Sec. III C. Following this, in Sec. IV we focus on the magnetic order at low temperatures through discussion of susceptibility, pulsed-field magnetization and neutron powder diffraction results. In Sec. IV C we discuss the implications of the monoclinic symmetry for the low-energy spin excitations and in Sec. V we present results of *ab-initio* electronic structure calculations. Finally, conclusions are summarized in Sec. VI.

II. METHODS

Crystals of $\alpha\text{-RuCl}_3$ were grown by vacuum sublimation from commercial RuCl_3 powder (Sigma Aldrich, Ru content 45-55%) sealed in a quartz ampoule and placed in a three-zone furnace with the end temperatures 650 and 450°C. Those temperatures were chosen in order to obtain phase-pure $\alpha\text{-RuCl}_3$ (the β polytype transforms irreversibly into the α phase above 395°C [Ref. 24]) and to ensure that the Cl_2 gas pressure in the ampoule did not exceed atmospheric pressure. The grown polycrystalline samples contained many flat-plate crystal pieces, often with a hexagonal shape and up to 1 mm in diameter. Single crystal x-ray diffraction in the range 80-300 K (under N_2 gas flow) was performed on many of those crystal

platelets using a Mo-source Oxford Diffraction Supernova diffractometer.

Magnetometry measurements were made under static fields using both a Quantum Design Magnetic Properties Measurement System (MPMS) and vibrating sample magnetometer (VSM). Pulsed-field magnetization experiments were performed on a stack of aligned crystal platelets in both $\mathbf{H} \perp \mathbf{c}^*$ (field in the honeycomb layers) and $\mathbf{H} \parallel \mathbf{c}^*$ (field normal to honeycomb layers) geometries. We employed an improved version of the setup described in Ref. 33, placed within a ^3He cryostat with a base temperature of 0.4 K and the 60 T short-pulse magnet at NHMFL Los Alamos.³⁴ The magnetization values measured in the pulsed-field experiments were calibrated against VSM data collected on the same sample.

Neutron powder diffraction measurements to obtain information about the magnetic structure were performed using the time-of-flight diffractometer WISH at the ISIS Facility in the UK. Approximately 5 g of powder $\alpha\text{-RuCl}_3$ (extracted from the crystal growth ampoule described above) was placed in an aluminium can and mounted in a standard helium-4 cryostat with a base temperature of 2 K. Additional measurements were performed using a closed-cycle refrigerator with a base temperature of 6 K.

The electronic structure calculations were performed with the all electron full potential Wien2k code.³⁵ We set the basis-size controlling parameter RK_{max} equal to 8 and considered a mesh of $8 \times 6 \times 8$ \mathbf{k} points in the first Brillouin zone (FBZ) for the self-consistency cycle. The density of states were calculated with $12 \times 12 \times 12$ \mathbf{k} points in the FBZ. All calculations were doubled checked with the FPLO code.³⁶

III. CRYSTAL STRUCTURE

A. Space group and stacking faults

The x-ray diffraction pattern was measured for many crystal platelets extracted from several growth batches. In all samples studied (over fifty), one could invariably observe sharp reflections and weak diffuse scattering in rods along the direction surface normal to the crystal plates, as characteristic of a layered crystal structure with stacking faults.³⁷ The positions of the sharp Bragg reflections could be consistently indexed by a monoclinic unit cell with space group $C2/m$ both at room temperature and the lowest temperature measured (80 K) with lattice parameters given in Table I. Some samples were found to have a single structural domain, some were found to contain two monoclinic twins rotated by $\approx 120^\circ$ about the direction normal to the plates (\mathbf{c}^*), and other samples contained multiple structural domains. For the un-twinned crystals the diffraction patterns had the empirical selection rule for observed Bragg peaks $h+k = \text{even}$, as characteristic of C-centering in the ab plane, and the peak intensities were symmetric under a 2-fold rotation around \mathbf{b}^* and mirror-plane reflection normal to \mathbf{b}^* , as expected

for a $2/m$ Laue class. The highest symmetry space group consistent with the above information is $C2/m$.

Representative data at 300 K from an un-twinned crystal (of $\approx 80\mu\text{m}$ diameter) is shown in Fig. 1D-F, for various diffraction planes. Note that all sharp Bragg peaks are in good agreement with calculations (panels G-I) for a $C2/m$ structure. In addition to sharp Bragg peaks, rods of diffuse scattering are also clearly visible along l (see panels E-F), with the general selection rule $k = 3n+1$ or $3n+2$ (n integer) and $h+k = \text{even}$ (due to C-centering). Diffuse scattering with the same selection rule was also observed in Na_2IrO_3 and attributed to faults in the stacking sequence of honeycomb $\text{Na}_{1/2}\text{IrO}_3$ layers.¹¹ By analogy, we attribute the above diffuse scattering observed in $\alpha\text{-RuCl}_3$ as originating from occasional shifts in the ab plane by $\pm \mathbf{b}/3$ between stacked RuCl_3 honeycomb layers. The intensities of the sharp Bragg peaks located at integer l positions on those diffuse scattering rods are expected to have a reduced intensity compared to a fully-ordered structure due to some transfer of intensity into the diffuse rod.³⁷ For the quantitative structural refinement we will show that it is helpful to distinguish between different families of Bragg peaks, and for this purpose we label the above family of Bragg peaks whose intensities are affected by diffuse scattering from sliding stacking faults as in Na_2IrO_3 , as ‘SFa’ (peaks affected by Stacking Faults of type ‘a’, to distinguish them from another family of type ‘b’, to be discussed below).

Upon cooling to low temperatures (80 K) no new diffraction peaks appear, but a second family of diffuse scattering rods becomes apparent. This is most clearly seen by comparing Figs. 1A and D, note the diffuse scattering rod near $(2,0,-2)$ (panel A, labelled peak position), which is prominent at low temperature, but only just visible at 300 K (panel D). Note also in Fig. 1C the strong diffuse scattering along $(1, \pm 3, l)$ positions, almost absent at 300 K (panel F). This type of diffuse scattering was not detected at 300 K in Na_2IrO_3 [Ref. 11] and has a different selection rule ($k = 3n$ and $h = 3m+1$ or $3m+2$ with n, m integers and $h+k = \text{even}$) compared to the diffuse scattering of type ‘a’ discussed previously. At 80 K both families of diffuse scattering rods have comparable intensities (see Fig. 1C). As before, the Bragg peaks located at integer l positions on this second family of diffuse scattering rods are expected to be reduced in intensity compared to a fully-ordered structure. We label this family of Bragg peaks as ‘SFb’ (peaks affected by Stacking Faults of type ‘b’).

Finally, a third family of Bragg peaks exist that are sharp at all temperatures measured, such as $(00n)$ (n integer) in Fig. 1A, so appear not to be affected by the presence of stacking faults. These have the general reflection condition $h = 3m$ and $k = 3n$ (n, m integers and $h+k = \text{even}$), and we label them ‘NSF’ (peaks Not affected by Stacking Faults).

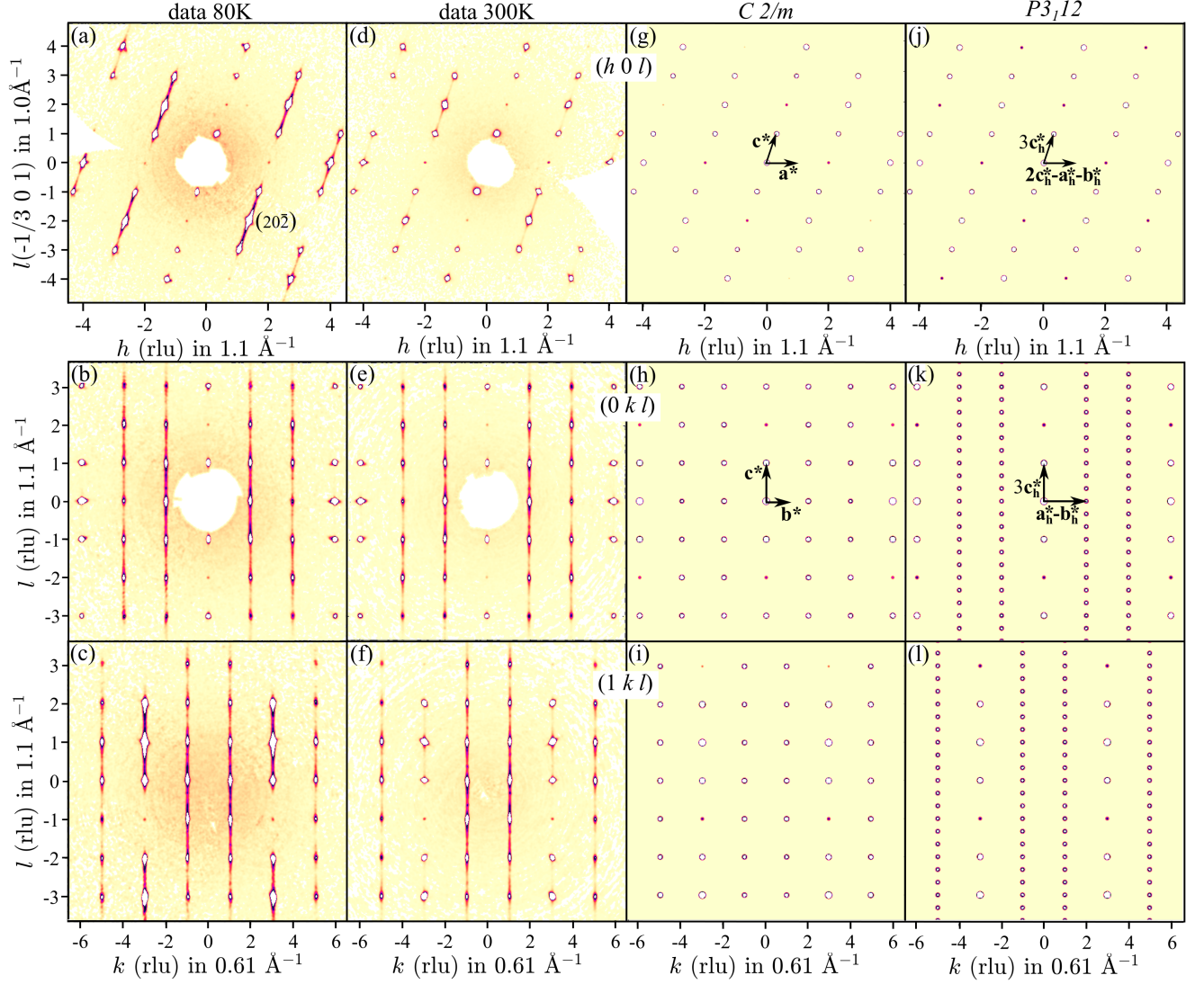


FIG. 1. (Color online) Observed x-ray diffraction patterns (log intensity scale) for an un-twinned crystal of α - RuCl_3 at 80 K (A-C), 300 K (D-F), shown for three different planes, compared with calculations (G-I) for the monoclinic $C2/m$ structural model (Fig. 2) and the trigonal $P3_112$ model (J-L). All wavevectors are labelled in r.l.u. units of the monoclinic cell and \mathbf{a}_h^* , \mathbf{b}_h^* and \mathbf{c}_h^* denote reciprocal lattice vectors of the hexagonal primitive cell of the trigonal structure (for the relation between the hexagonal and monoclinic axes see Sec. III C). Note the sharp peaks in the data are in good agreement with the monoclinic model (compare D-F with G-I), whereas the “supercell” peaks expected in the case of the trigonal model (K-L) at fractional positions $l = n + 1/3, n + 2/3$ (n integer) are clearly absent from the data, instead only diffuse scattering is found in those places.

B. Structural refinement at 80 K

To obtain a reference, fully-ordered 3D structure with no stacking faults we must refine a structural model against only those diffraction peaks that are unaffected by the presence of stacking faults. These are the family labelled NSF, as defined above. In the following, we focus primarily on the data collected at 80 K. Out of a total 1451 Bragg peaks measured, 135 are NSF peaks, of those just 32 are symmetry inequivalent after data reduction in space group $C2/m$. Despite the small number

of reflections a full refinement using FULLPROF³⁸ of a structural model, with starting atomic positions for Ru and Cl taken to be those of Ir and O in the structure of Na_2IrO_3 , converged well. Hence, the data was found to be fully consistent with the same structural motif as that found in Na_2IrO_3 with honeycomb layers of edge-sharing RuCl_6 octahedra stacked vertically with an in-plane offset (see Fig. 2), with Ru in place of Ir, Cl in place of O, and removing Na altogether. However, detailed tests showed that the refinement was in fact not sufficiently sensitive to the y -position of the Ru ion, or

TABLE I. α - RuCl_3 crystal structure parameters at 80 K.

Cell parameters				
Space group: $C2/m$				
$Z = 4$				
a, b, c (\AA)	5.9762(7)	10.342(1)	6.013(1)	
α, β, γ ($^\circ$)	90	108.87(2)	90	
Volume (\AA^3)	371(2)			
Atomic fractional coordinates from DFT				
Atom	Site	x	y	z
Ru	4g	0	0.33441	0
Cl1	8j	0.75138	0.17350	0.76619
Cl2	4i	0.73023	0	0.23895
Selected bond lengths and angles from DFT				
$\text{Ru}_1\text{-Ru}_2$	3.42513 \AA			
$\text{Ru}_2\text{-Ru}_3$	3.46080 \AA			
$\text{Ru}_1\text{-Cl2-Ru}_2$	92.5954 $^\circ$			
$\text{Ru}_2\text{-Cl1-Ru}_3$	93.9310 $^\circ$			
Fitted isotropic atomic displacement parameters				
Atom	$U_{iso}(\text{\AA}^2)$			
Ru	0.005(1)			
Cl1	0.006(2)			
Cl2	0.006(2)			
Data collection				
	SFa	SFb	NSF	
# measured refl.	991	325	135	
# independent refl.	189	68	32	
$R_{\text{int}}(C2/m)$	8.0%	3.3%	2.9%	
Fit to NSF peaks				
(Criterion for observed reflections: $I > 3.0\sigma(I)$)				
# observed reflections:	32			
# fitted parameters:	3			

the precise distortions of the Cl_6 octahedra, so the internal atomic fractional coordinates could not be uniquely determined from the x-ray data alone. The atomic positions are key to understanding the underlying physics as the exchange interactions (and their anisotropy) are expected to be strongly dependent on the geometry of the Ru-Cl-Ru bonds. So to construct a robust structural model we use *ab-initio* density functional theory (DFT) calculations to predict the atomic positions that give the lowest energy ground state using as input the experimentally determined space group and lattice parameters, and then check consistency of this constrained structural model with the intensities in the x-ray diffraction data. For the DFT structural relaxation calculations

we employed the projector augmented wave method as implemented in the VASP package³⁹ with the generalized gradient approximation (GGA)⁴⁰, as well as the full potential local orbital (FPLO) method.³⁶

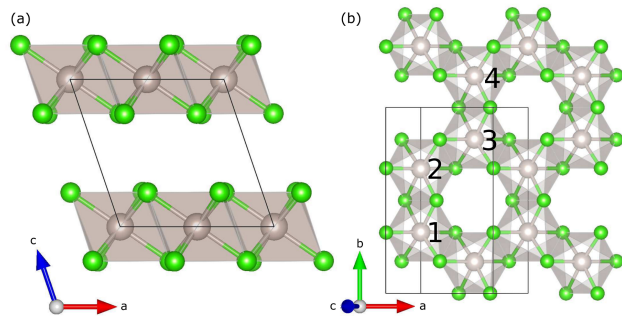


FIG. 2. (Color online) Monoclinic crystal structure of α - RuCl_3 , showing the unit cell as a black outline, Ru as grey balls and Cl as green. (a) Projection onto the ac plane. (b) Basal layer projected onto the ab plane.

The atomic fractional coordinates predicted by DFT within the above empirical constraints are given in Table I. The refinement of the structural model against the 80 K NSF peak intensities was repeated with atomic fractional coordinates fixed to those DFT values, with only isotropic displacement parameters and a global scale factor left free to vary. A reliability factor of $R_{F^2} = 4.2\%$ was obtained, which compared to a value of $R_{F^2} = 3.7\%$ achieved for the completely free refinement (when atomic coordinates were also allowed to vary), demonstrates that the theoretically predicted atomic coordinates are fully consistent with the x-ray diffraction data. Fig. 3 shows the observed structure factors squared, $|F|^2$, for all families of diffraction peaks compared to those calculated from the fit against only the NSF peaks. The excellent agreement with the NSF peak intensities at 80 K is clear (Fig. 3b, black symbols). Furthermore, one can see that intensities of both SFa (blue) and SFb (red) peaks are systematically overestimated, consistent with the expectation that some of their nominal intensity has been transferred into the diffuse scattering in their vicinity. Fig. 3a shows the same fit, but performed against the room temperature data set (with empirically-determined lattice parameters $a = 5.9856(4)\text{\AA}$, $b = 10.3557(5)\text{\AA}$, $c = 6.0491(4)\text{\AA}$, $\beta = 108.828(7)^\circ$ and assuming atomic fractional coordinates fixed to the DFT predicted values listed in Table I). Even at this temperature, the structural model agrees well with the x-ray data ($R_{F^2} = 5.5\%$ for NSF peaks), and the intensities of the SFb peaks (red symbols) appear to be also almost quantitatively reproduced by the model, as at this temperature the diffuse scattering near SFb peaks is almost absent, so the intensity of SFb peaks is expected to be only very weakly reduced compared to a perfectly-ordered structure.

The obtained crystal structure allows us to naturally understand the strong periodic modulations in the inten-

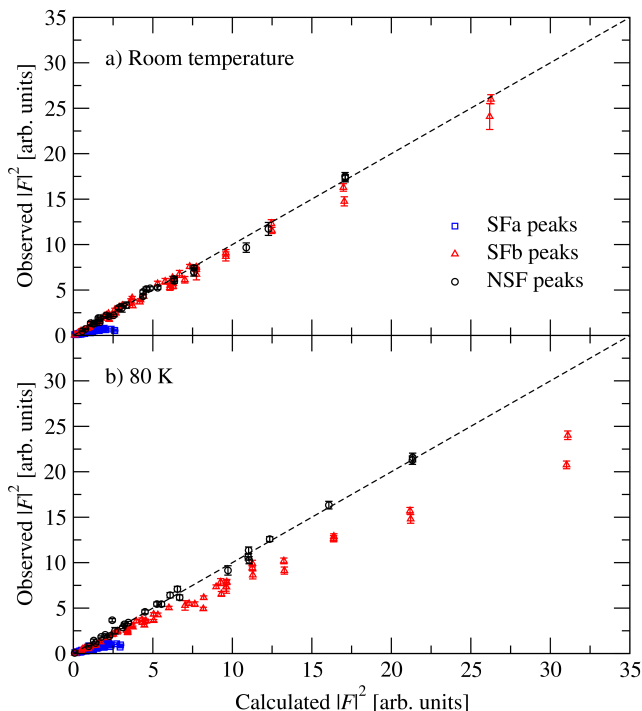


FIG. 3. (Color online) Observed structure factor squared values of all three families of diffraction peaks compared to those calculated by fitting the $C2/m$ monoclinic structural model with fixed theoretical atomic fractional coordinates to data measured at a) room temperature, and b) 80 K.

sity of x-ray diffraction peaks, in particular the rather conspicuous period-4 repeat in the intensity of peaks along l in the $(h0l)$ plane (see Fig. 1D) with almost extinct peaks at $(0,0,\pm 2)$ and $(\pm 2,0,0)$ positions. The near-absence of intensity at those positions is due to an almost total cancellation of the scattering from the Ru ion with that from the three Cl ions with atomic scattering amplitudes $f_{\text{Ru}} : f_{\text{Cl}}$ in ratio almost 3 : 1. In detail, the Ru ion is located at $z = 0$, whereas the Cl ions are at $z \simeq 1/4$ and $3/4$ (see Table I), so the structure factors for $(00l)$ reflections follow (to a good approximation) a period-4 sequence of values $f_{\text{Ru}} + 3f_{\text{Cl}}$, f_{Ru} , $f_{\text{Ru}} - 3f_{\text{Cl}}$, f_{Ru} , $f_{\text{Ru}} + 3f_{\text{Cl}} \dots$. In the limit of small wavevectors \mathbf{Q} , the atomic scattering factors are given by the number of electrons, so $f_{\text{Ru}} : f_{\text{Cl}} = 44 : 17 \approx 3 : 1$, such that to good approximation the structure factors are multiples of 4, 1, 0, 1, 4... for $l = 0, 1, 2, 3, 4 \dots$. Similarly, one can show that a period-4 modulation in intensity along l occurs in general for $(h0l)$ peaks, with zeros at $h + l = 4n + 2$ (n integer and h even) explaining all the near-extinctions and apparent intensity modulations seen in Fig. 1D. We note that such near extinctions do not occur in the diffraction pattern of the iso-structural Na_2IrO_3 , as the scattering factors of Ir and O are much more anisotropic (ratio almost 10:1) and Na is also contributing to the diffraction peak intensities.

To summarize, the x-ray diffraction patterns uniquely

identify the monoclinic $C2/m$ space group both at room temperature and the lowest temperature measured (80 K), and quantitative structural refinement using fixed atomic fractional coordinates predicted by DFT, performed only against the sharp diffraction peaks whose intensity is not affected by the presence of stacking faults, gives a very good description of the data. The corresponding crystal structure is shown in Fig. 2 and consists of monoclinically-stacked RuCl_3 honeycomb layers as in AlCl_3 [Ref. 31] and Na_2IrO_3 . The real materials are understood to have occasional stacking faults with respect to this reference monoclinic structure.

C. Other Structural Models

The current structural model assumed for $\alpha\text{-RuCl}_3$ (trigonal space group $P3_112$ [Ref. 27], conventionally described in a hexagonal unit cell) differs from the monoclinic $C2/m$ structure primarily in the stacking sequence of the honeycomb layers, with a three-layer stacking periodicity as opposed to single layer in $C2/m$. We note that the dimensions of the unit cell are, in general, an insufficiently robust criterion to reliably distinguish between those two structural models as the monoclinic unit cell metric is in fact very close to hexagonal, i.e. $b \simeq \sqrt{3}a$ to within better than 0.2%, and $3c \times \cos \beta \simeq -a$ to within 2%. When the latter equation is satisfied exactly one has eclipsed (straight-on-top) stacking at the 3rd honeycomb layer, so an alternative hexagonal cell with a 3-layer periodicity along the direction normal to the layers could in principle provide an approximate metric to index the positions of Bragg diffraction peaks. In this case the transformation between the hexagonal (subscript h) and symmetrized monoclinic unit cell vectors (subscript m) is given by $\mathbf{a}_m = -\mathbf{a}_h - \mathbf{b}_h$, $\mathbf{b}_m = \mathbf{a}_h - \mathbf{b}_h$, $\mathbf{c}_m = (\mathbf{a}_h + \mathbf{b}_h + \mathbf{c}_h)/3$, where $a_m = a_h$, $b_m = \sqrt{3}a_h$, $\beta = \pi/2 + \text{atan}(a_h/c_h)$, and $c_m = c_h/(3 \sin \beta)$.

However, the internal atomic arrangement in the monoclinic and trigonal structures is different due to the distinct symmetries of the corresponding space groups, and these differences would be directly observed in the measured single crystal diffraction patterns. In particular, the two structures have a distinct stacking sequence of the honeycomb layers: for two adjacent layers both the symmetrized monoclinic and trigonal structures would appear identical, but for every subsequent layer in the trigonal structure the direction of the in-plane offset (defined by the monoclinic angle, β) would rotate by 120° around the direction normal to the layers. The resulting 3-layer stacking periodicity in the trigonal structure would lead to the appearance of extra *supercell* peaks along the \mathbf{c}^* -axis, which, in the monoclinic basis, would occur at non-integer positions $l = n + 1/3$ and $n + 2/3$ ($k = 3m + 1$ or $3m + 2$, and $h + k = \text{even}$ with h, m, n integers) in addition to, and with the same intensity as, the nominal peaks at integer $l = n$ positions (see Fig. 1K-L). The absence of supercell peaks in our diffraction

data [compare Fig. 1E-F with K-L) conclusively rules out the proposed $P3_12$ model. For completeness, we note that an alternative rhombohedral stacking sequence of the honeycomb layers with space group $R\bar{3}$ proposed¹⁹ for α - RuCl_3 by analogy with the low-temperature phase of CrCl_3 [Ref. 41], also has a 3-layer stacking periodicity so would also predict supercell peaks at non-integer $l = n + 1/3$ and $n + 2/3$ positions, not observed in the data, so this rhombohedral structure can similarly be ruled out for the crystals studied here.

We note that if a sample contained three monoclinic twins of equal weight and rotated by 120° around \mathbf{c}^* , then there would be no striking qualitative difference between the diffraction pattern from monoclinic and trigonal/rhombohedral structural models. Furthermore, under the symmetry constraints of those candidate structures there would be only slight variations in intensity due to differences in the displacements of the Cl or Ru ions from their idealized positions, which are expected to be small and likely below the experimental sensitivity. As such, measuring un-twinned crystals has proved to be crucial in the present study to qualitatively, and quantitatively, determine the correct monoclinic reference structure for the samples reported here.

IV. MAGNETIC PROPERTIES

A. Susceptibility and magnetization

The magnetic susceptibility of a stack of single crystals representative of those used in our structural study (Sec. III), and a 12.8 mg powder, was measured on heating (after zero-field cooling) from 2 K up to 300 K. Only a single anomaly was observed for both samples near 13 K [see Fig. 4a], which is indicative of long-range antiferromagnetic ordering of the ruthenium magnetic moments. Our powder data is fully consistent (in absolute units) with data previously reported on powder α - RuCl_3 samples.²⁵ Previous single crystal studies have reported two magnetic transitions near 8 and 14 K [Refs. 17, 19, and 20], which have been attributed to either a mixture of two coherent stacking orders, with each order associated with a single transition, respectively,¹⁸ or alternatively to a single phase that supports an unexpected magnetic ground state.¹⁷ Here, to the contrary, we find that the low-field magnetic susceptibility of single crystals is consistent with that of the powder, both displaying a single transition to magnetic order at low temperatures.

Pulsed-magnetic-field $M(H, T)$ data are shown for field sweeps up to 15 T at various constant temperatures T in Fig. 5b. The data shown was recorded during the rising part of the field pulses; $M(H)$ curves from the rising and falling portions of the field pulse were indistinguishable within the limit of experimental sensitivity (*i.e.* there was little or no hysteresis). For $\mathbf{H} \perp \mathbf{c}^*$ the low-temperature $M(H)$ curves show a pronounced steep-

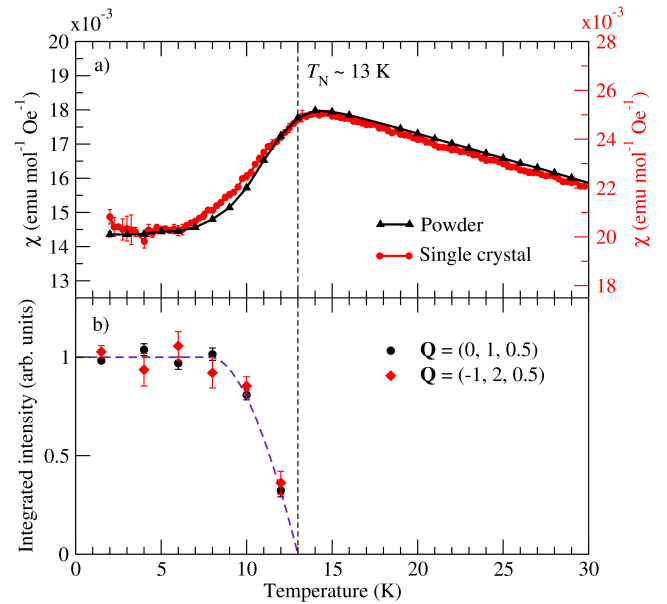


FIG. 4. (Color online) a) Magnetic susceptibility as a function of temperature for a stack of single crystals (red circles, $\mathbf{H} \perp \mathbf{c}^*$) representative of those used in the x-ray diffraction experiments described in Sec. III, and the powder sample used in the neutron diffraction experiments discussed in Sec. IV B (black triangles), in a magnetic field $H = 1000$ Oe. b) Temperature dependence of the integrated intensity of the two magnetic reflections observed in neutron powder diffraction pattern in Fig. 7, normalized to an average of unity at low temperatures. The dashed line is a guide to the eye.

ening at about 8 T, characteristic of a field-induced phase transition, which gradually shifts down in field and fades as the temperature increases. This trend is more clearly seen in the full phase diagram shown in Fig. 5a), which displays maximum values (solid symbols) of the differential susceptibility (dM/dH) as a function of H and T . The inset to Fig. 5a) shows complementary $M(H, T)$ data recorded in the VSM as temperature sweeps in fixed field. The same transition is seen as a peak in $M(T)$ that disappears at fields above 8 T. This trend is also drawn in the main pane of Fig. 5a), which completes a continuous phase boundary (dashed line) consistent with a single enclosed antiferromagnetic phase for α - RuCl_3 at low temperatures and modest magnetic fields applied in the honeycomb layers.

The pulsed-field data shown in Fig. 5b) for $\mathbf{H} \parallel \mathbf{c}^*$ exhibit $M(H, T)$ values that are a factor 5–6 times smaller than those recorded on the same sample under comparable conditions for $\mathbf{H} \perp \mathbf{c}^*$. This is likely to be due to Ru g -factor anisotropy.¹⁹ Note that there is no sign of the phase transition observed in the other field orientation, leading us to conclude that it is a feature observed only when the field lies in the honeycomb plane.

Having measured the magnetization along the two non-equivalent directions on the *same* sample enables us to reliably put both data sets in absolute units by cali-

bration against the susceptibility data measured on a powder sample [Fig. 4a) black symbols] under the same conditions of applied field and temperature, thus avoiding the inherent uncertainties associated with measuring the precise mass of very small (of order ~ 0.1 mg) crystals. The powder susceptibility is expected to reflect the spherically-averaged value, obtained as $\chi_{\text{powder}} = (2/3)\chi_{\parallel} + (1/3)\chi_{\perp} = \chi_{\parallel}(2+r)/3$, where $r = \chi_{\perp}/\chi_{\parallel}$ is the susceptibility anisotropy. The single crystal data sets in Figs. 4a) (red symbols) and Fig. 5b-c) were then scaled to satisfy the above relations with the powder susceptibility data at $\mu_0 H = 0.1$ T and 15 K, where the susceptibility anisotropy under those conditions was obtained as $r = 0.157$ from the pulsed field data.

Fig. 5c) shows $M(H, T)$ data recorded in 60 T pulsed-field shots; as is the case with the lower-field data, there is little or no hysteresis between up- and down-sweeps of the field, and so, for clarity, only data recorded on the rising part of the field pulse are shown. The $M(H)$ anisotropy persists to high fields, though the data for $\mathbf{H} \perp \mathbf{c}^*$ show signs of the approach to saturation. There are no further phase transitions visible up to 60 T in either field direction.

The shape of the magnetization curve at high field as observed by the upper traces in Fig. 5c) with a gradually decreasing differential susceptibility upon increasing field suggests an asymptotic approach to magnetization saturation. Such a behaviour of the magnetization near saturation is commonly seen^{42,43} when the spin Hamiltonian does not have rotational symmetry around the applied field direction. In this case the total spin along the field direction $S_T^{\xi} = \sum_i S_i^{\xi}$ is not a good quantum number (the operator does not commute with the spin Hamiltonian $[S_T^{\xi}, \mathcal{H}] \neq 0$, where ξ denotes the direction of the applied field \mathbf{H} and i runs through all the magnetic sites) and as a consequence even in the limit of very high fields quantum fluctuations are still present and reduce the magnetization from its fully-available value, with saturation strictly reached only in the asymptotic limit of infinite field. This is qualitatively different from the case when the spin Hamiltonian does have rotational symmetry around the field direction, for example the case of purely Heisenberg interactions, $\mathcal{H} = \sum_{ij} J_{ij} \mathbf{S}_i \cdot \mathbf{S}_j$. In this case the total spin along the field direction is a good quantum number, magnetization saturation is an exact plateau phase where quantum fluctuations are entirely absent, and the approach to magnetization saturation from below is via a sharp phase transition at a critical field H_C , with the susceptibility in general increasing upon increasing field up to H_C , then being strictly zero above it. The observed shape of the magnetization curve at high field (upper traces in Fig. 5c) is consistent with the former scenario with an asymptotic approach to saturation and could be taken as evidence for the presence of strongly anisotropic, non-Heisenberg exchanges in α -RuCl₃, of Kitaev⁴³ or another strongly-anisotropic form.

B. Magnetic Neutron Powder Diffraction

Neutron powder diffraction data were collected deep in the ordered phase (6 K) and in the paramagnetic region (20 K) with high counting statistics to allow a quantitative refinement. Additional data to monitor the temperature dependence and extract an order parameter was collected with lower statistics at 2 K intervals in the range 2-14 K. Fig. 7 shows the purely magnetic contribution to the neutron diffraction pattern at 6 K obtained after subtracting off the 20 K paramagnetic pattern. Two clear magnetic diffraction reflections are observed at d -spacings $d = 3.88$ and 7.67 Å. The integrated intensity of the two reflections is plotted as a function of temperature in Fig. 4b. Both peaks show the same temperature dependence, and clearly demonstrate the onset of long-range magnetic order below $T_N \approx 13$ K. Furthermore, both magnetic susceptibility and neutron diffraction data are consistent with a single magnetic ordered phase down to the lowest temperature measured (2 K).

Both magnetic reflections could be indexed with the propagation vector $\mathbf{k} = (0, 1, 0.5)$ with reference to the $C2/m$ structural unit cell. This finding alone provides key information on the ground state magnetic structure of our α -RuCl₃ samples. The value $k_z = 0.5$ determines that the magnetic moments in neighbouring honeycomb layers are aligned antiferromagnetically. Within a honeycomb layer there are four symmetry equivalent ruthenium ions per unit cell, labelled 1-4 in Fig. 2b) and Fig. 6. The four sites can be considered as two pairs of sites, (1 and 2) and (3 and 4), intra-related by mirror symmetry operations at $(x, \frac{1}{2}, z)$ and $(x, 0, z)$, respectively, and inter-related by the C -centering translation vector $\mathbf{t} = (\frac{1}{2}, \frac{1}{2}, 0)$. The relative orientation of the magnetic moment pairs, (1 and 2) and (3 and 4), is uniquely determined by the phase $2\pi\mathbf{k} \cdot \mathbf{t}$, *i.e.* for $k_x = 0$ and $k_y = 1$ the two pairs are aligned antiferromagnetically. Furthermore, for this \mathbf{k} -vector the relative orientation of moments within a given pair is strictly parallel or antiparallel by symmetry, however these two scenarios are not differentiated by the propagation vector alone and must be tested against the diffraction data. For parallel alignment within each pair the resulting magnetic structure is a ‘stripy’ antiferromagnet with spins forming ferromagnetic stripes (ladders) along a alternating in orientation along b . In the case of antiparallel alignment within each pair the magnetic structure consists in ‘zigzag’ ferromagnetic chains along a arranged in an antiferromagnetic pattern along b , as illustrated in Fig. 6. Symmetry analysis performed using BasIreps, part of the FULLPROF package,³⁸ for the propagation vector \mathbf{k} gives magnetic basis vectors containing moments aligned along the b -axis (the unique 2-fold axis of the crystal structure) or in the ac plane. If the transition from paramagnetic to magnetic order is continuous then the magnetic structure would be expected to adopt just one of those two configurations, which can be directly tested by the magnetic diffraction data.

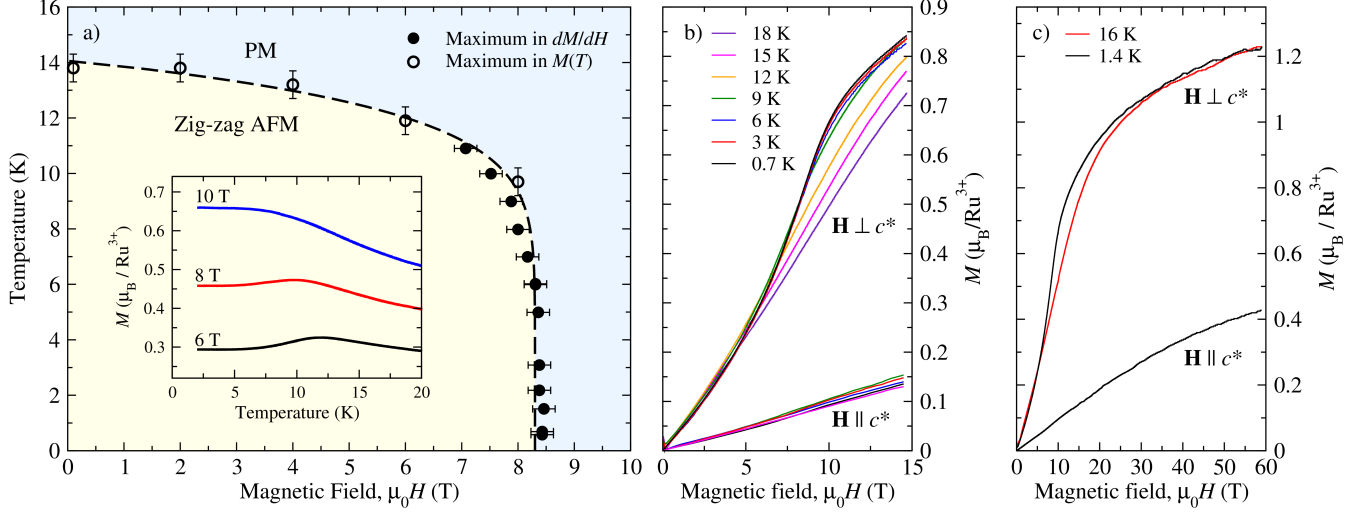


FIG. 5. (Color online) a) Magnetic phase diagram for single crystal α - RuCl_3 in magnetic field $\mathbf{H} \perp \mathbf{c}^*$. Solid points mark the maxima in the differential susceptibility dM/dH derived from data shown in panel b) (upper traces). Open symbols mark the maximum in $M(T)$ VSM temperature sweeps, as shown in the pane inset for constant magnetic field values close to the phase boundary. The dashed line is a guide to the eye phase boundary between the zigzag antiferromagnetic phase (yellow shading) and paramagnetic (PM, blue shading). b) $M(H, T)$ data recorded in the rising part of 15 T field pulses at a series of constant temperatures. At lower temperatures, the steep rise in $M(H)$ is strongly suggestive of a field-induced phase transition near 8 T. c) $M(H, T)$ data recorded in the rising part of 60 T field pulses in both the antiferromagnetic and paramagnetic phases.

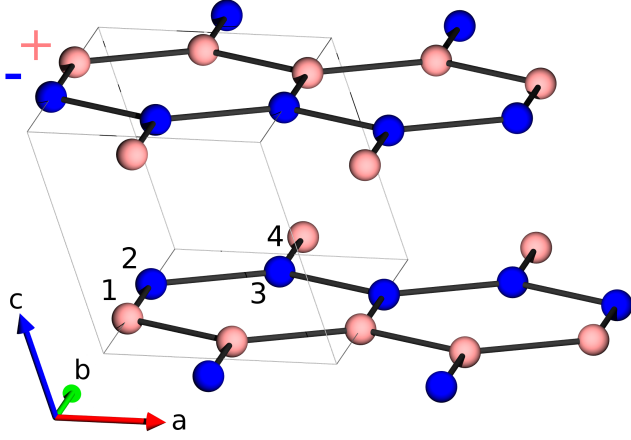


FIG. 6. (Color online) The zigzag magnetic structure of α - RuCl_3 . The magnetic moments of ruthenium atoms colored red and blue are aligned antiparallel and oriented within the ac -plane. Ru-Ru connections are drawn in thick black lines to illustrate the honeycomb layers, and the $C2/m$ monoclinic unit cell is drawn in thin gray lines.

The two magnetic reflections observed in the difference diffraction data in Fig. 7 at $d = 3.88$ and 7.67 Å are indexed as $(-1, 2, 0.5)$ and $(0, 1, 0.5)$, respectively. The peak at higher d -spacing was found to be significantly broader than that at 3.88 Å. We assign this broadening to the effects of stacking faults, as discussed above. Without a fully quantitative model of the stacking faults we cannot rule out the possible existence of otherwise un-

observed weak magnetic reflections close to background levels. However, all statistically significant reflections can be fit using a peak specific broadening model, hence allowing for the zigzag and stripy models, and the moment direction, to be tested.

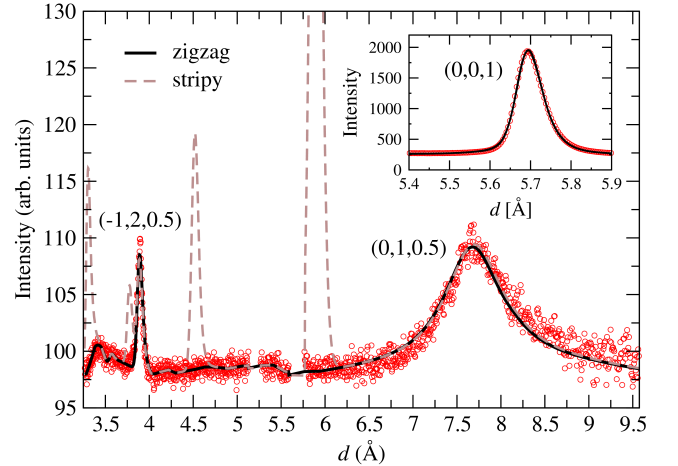


FIG. 7. (Color online) Neutron powder diffraction data measured at 6 K, with the 20 K paramagnetic data subtracted. The diffraction pattern for both zigzag (black solid line) and stripy (brown dashed line) models are calculated and plotted for a moment oriented along \mathbf{c}^* , a similar level of agreement for the zigzag structure could be obtained for a general moment direction in the ac plane. Inset: fit to the (001) nuclear Bragg reflection, unaffected by stacking faults, used for calibrating the magnetic diffraction intensities.

The solid and dashed lines in Fig. 7 show the calculated diffraction patterns for both magnetic structures. In both cases the relative intensity of the two observed reflections could only be reproduced with magnetic moments oriented within the ac -plane, however, within experimental uncertainties the fit to the data was not sufficiently sensitive to the precise moment direction in this plane. Furthermore, one can immediately rule out the stripy model (dashed line), which predicts strong magnetic reflections for any moment direction at d -spacing positions where no such reflections are observed in the data, beyond any ambiguity inherent to peak broadening effects. To estimate the ordered Ru magnetic moment magnitude we calibrate the magnetic diffraction intensities against the (001) nuclear reflection (Fig. 7 inset), which is unaffected by stacking faults (see Sec. III), and fit the Ru moment magnitude within the zigzag model (black line in Fig. 7). In the fit to the reference (001) structural peak only an intensity scale factor was varied with all the internal crystal structure parameters kept fixed to the values at 80 K (Table I), only adjusting for the effect of the lower temperature in the neutron measurements by a slight reduction in the lattice parameters, estimated by fitting the nuclear peak positions observed in the neutron diffraction data at low d -spacing (not shown). Using this procedure we find the lower limit for the magnetic moment to be $0.64(4) \mu_B$, with the actual value being dependent on the precise moment direction, which the present data only constraints to be in the ac plane. Despite not knowing the exact moment direction, the symmetry of the ground state magnetic structure is now well established as zigzag in-plane order with antiferromagnetic stacking along c , in qualitative agreement with previous studies.^{17,18} In monoclinic symmetry the magnetic structure is described by the magnetic super-space group C_c2/m , with basis transformation $[[1,0,2],[0,-1,0],[0,0,-2]]$ and origin shift $(-1/2,0,-1/2)$ with respect to the parent $C2/m$ unit cell.

C. Implications of Monoclinic Symmetry for the Magnetic Exchange Interactions

Here we discuss possible implications of the monoclinic crystal structure for the low-energy spin excitations in the magnetically ordered phase. Recent inelastic powder neutron scattering measurements have reported¹⁸ dispersive magnetic excitations above a gap of ≈ 1.7 meV and it was proposed that features observed in the inelastic spectrum at intermediate energies above this gap could be understood based on a minimal Kitaev-Heisenberg model on the honeycomb lattice, with an antiferromagnetic Kitaev exchange K and a ferromagnetic Heisenberg term J . However, it was pointed out that this minimal model could not account for the observed spin gap, as for a honeycomb lattice with full three-fold symmetry (as expected in the trigonal $P3_112$ structural model) the exchanges along the three bonds meeting at each lattice site are

symmetry-equivalent, and in this case linear spin-wave theory predicts a gapless spectrum,¹⁸ contrary to that observed experimentally. We note that the $C2/m$ monoclinic structure breaks the symmetry between the three bonds in the honeycomb planes, making the b -axis bond non-equivalent to the other two bonds, which remain symmetry-equivalent; this opens the possibility that the magnitude of the anisotropic exchange could be different between the two families of bonds. By repeating the linear spin-wave calculations reported in Ref. 18 we find that an anisotropy of order 10% in the magnitude of the Kitaev term between the two families of bonds (larger in magnitude for the b -axis bond) would be sufficient to account for the magnitude of the observed spin gap, suggesting that non-equivalence between the different bonds in the honeycomb plane induced by the underlying monoclinic distortions may provide a natural mechanism to explain the observed spin gap.

V. ELECTRONIC STRUCTURE

Here we discuss the implications of the monoclinic crystal structure for the electronic band-structure and the magnetic ground state of the Ru ions. Within a honeycomb layer the difference in the atomic positions in the trigonal $P3_112$ [Ref. 27] compared to the monoclinic $C2/m$ models is on visual inspection minimal. However, subtleties of the crystal structure in fact have profound implications for the nature of the electronic structure. The trigonal crystal structure features shorter Ru-Ru bonds, and as a result the calculated electronic structure is dominated by Ru-Ru direct hopping. On the other hand, in the present monoclinic structure the dominant hopping process is one *via* Cl p states, which, as discussed in references⁴⁴⁻⁴⁶ for Na_2IrO_3 , leads to the formation of quasimolecular orbitals (QMO) that consist of a linear combination of t_{2g} states of the six Ru atoms in a hexagon.

In Fig. 8 we show the *nonrelativistic* density of states within GGA projected onto the QMO basis for $\alpha\text{-RuCl}_3$ in the $C2/m$ and $P3_112$ crystal structures, as well as that for Na_2IrO_3 for comparison. While $\alpha\text{-RuCl}_3$ ($C2/m$) and Na_2IrO_3 are predominantly diagonal in the QMO basis, this is not the case for $\alpha\text{-RuCl}_3$ ($P3_112$) as can be observed from the strong mixing of QMO states.

To analyze spin orbit and correlation effects we present in Fig. 9 the electronic structure of $\alpha\text{-RuCl}_3$ ($C2/m$) in the GGA, GGA+SO (GGA plus inclusion of spin-orbit effects) and GGA+SO+U (GGA plus inclusion of spin-orbit effects and on-site Coulomb repulsion U) approximations as implemented in Wien2k.³⁵ Here, an insightful comparison with Na_2IrO_3 may be drawn, as follows. In Na_2IrO_3 [Refs. 44 and 45] the combination of accidental degeneracy of the two highest QMOs, A_{1g} and E_{2u} , combined with strong spin-orbit coupling, largely destroys the QMO and leads instead to the formation of relativistic $j_{\text{eff}} = 1/2$ orbitals (the QMOs are still relevant as

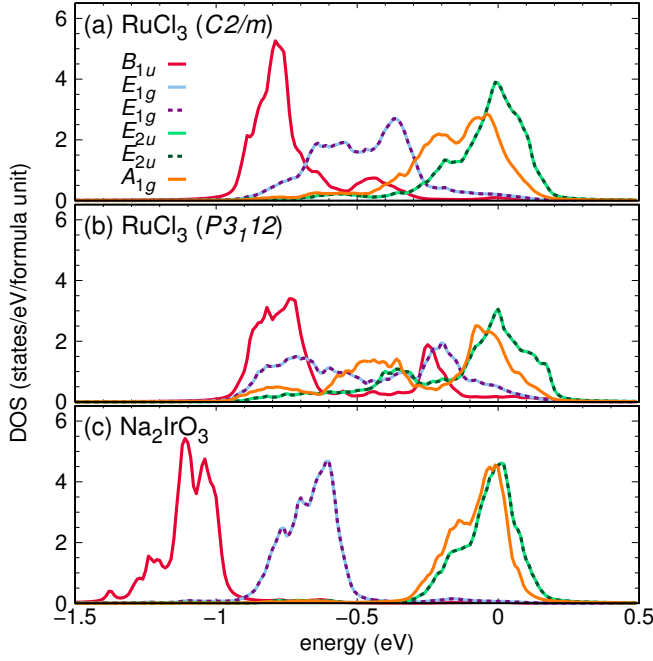


FIG. 8. (Color online) GGA density of states projected onto the quasi-molecular orbital basis of a) α -RuCl₃ in the $C2/m$ structure, b) α -RuCl₃ in the $P3_112$ structure²⁷ and c) Na₂IrO₃.

they generate unexpectedly large second and third neighbor magnetic interactions^{11,14}). Adding the Hubbard U in Na₂IrO₃ increases the band gap, but does not affect the electronic structure in any qualitative way. However, given that the spin-orbit coupling on Ru is much smaller than on Ir, turning on the spin-orbit coupling leaves the QMO picture in α -RuCl₃ ($C2/m$) almost intact (Fig. 9b). Interestingly, adding U dramatically changes the electronic structure (Fig. 9c). Such an addition effectively renormalizes the one-electron hopping by a factor of t/U and increases the effect of spin-orbit coupling that now becomes an important player. Eventually, the electronic structure with *both* spin-orbit and U looks surprisingly similar to that of Na₂IrO₃ [Refs. 44–46].

We emphasize that the physics leading to the formation of this electronic structure in the two systems is qualitatively different, which needs to be kept in mind when comparing physical properties of the two compounds. While without spin orbit and Hubbard correlation both systems are molecular-orbitals solids, and with inclusion of both effects the spin-orbit interaction takes control, in Na₂IrO₃ this happens because the spin-orbit coupling is initially strong, and correlations play a secondary role, in α -RuCl₃ ($C2/m$) the much stronger correlation conspires with spin orbit, which otherwise is too weak to overcome the one-electron hopping effects.

The GGA+SO+ U bandstructure for α -RuCl₃ ($C2/m$) can be projected onto the $j_{\text{eff}} = 1/2, 3/2$ basis as shown in the density of states in Fig. 9c). While there is some mixing between the two projections, $j_{\text{eff}} = 1/2$ has the

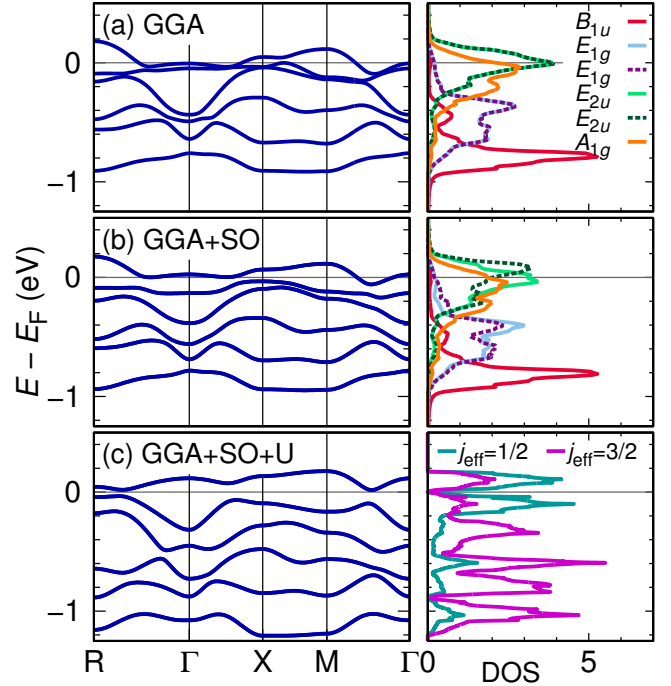


FIG. 9. (Color online) Band structure and density of states of α -RuCl₃ in the $C2/m$ structure obtained within (a) GGA, (b) GGA+SO, and (c) GGA+SO+ U ($U_{\text{eff}} = 3$ eV). The right panel shows the projected nonmagnetic GGA and GGA+SO density of states onto the quasi-molecular orbital basis^{44,45} and the GGA+SO+ U density of states onto the relativistic j_{eff} basis.

dominant contribution at the Fermi level. Therefore, a description of this system in terms of $j_{\text{eff}} = 1/2$ orbitals may still be valid. This is in qualitative agreement with GGA+SO+ U calculations reported for α -RuCl₃ in the $P3_112$ structure¹⁶ although the two electronic structures differ quantitatively.

VI. CONCLUSIONS

We have proposed a revised three-dimensional crystal structure for the layered honeycomb magnet α -RuCl₃ based on x-ray diffraction on un-twinned crystals combined with *ab-initio* structural relaxation calculations. In contrast with the currently-assumed three-layer stacking periodicity, we have found a single layer stacking periodicity with a monoclinic unit cell, iso-structural to Na₂IrO₃, with occasional faults in the stacking sequence. In powder neutron diffraction and in susceptibility measurements on both powders and single crystals we have observed a single magnetic transition near 13 K, and through analysis of the magnetic diffraction pattern we have confirmed that this phase has zigzag antiferromagnetic order. Using both static and pulsed magnetic field experiments we have observed that the zigzag phase is

suppressed by relatively small magnetic fields (≈ 8 T) applied in the honeycomb layers, whereas it is robust in fields applied perpendicular to the honeycomb layers. We have discussed how the monoclinic crystal structure could provide a natural mechanism to explain the spin gap observed in inelastic neutron scattering experiments and how the asymptotic shape of the magnetization curve at high fields near saturation is consistent with proposals for strongly-anisotropic (non-Heisenberg) magnetic interactions.

ACKNOWLEDGMENTS

We acknowledge useful discussions regarding pulsed field magnetometry with P. A. Goddard, and regarding electronic structure with G. Khaliullin and S. Winter. Work in Oxford was supported by EPSRC under Grants

No. EP/H014934/1, EP/J003557/1 and EP/M020517/1, and in Frankfurt by the Deutsche Forschungsgemeinschaft through grant SFB/TR49. A.A.H. acknowledges support from the Royal Society through an International Newton Fellowship and Y.L. acknowledges support from a China Scholarship Council (CSC) Fellowship. I.I.M. was supported by the Office of Naval Research through the Naval Research Laboratory's Basic Research Program. R.C. and R.V. were supported in part by KITP under NSF grant PHY11-25915. Work at LANL was supported by the U.S. Department of Energy (DoE) Basic Energy Science Field Work Proposal 'Science in 100 T'. The NHMFL facility at LANL is funded by the National Science Foundation Cooperative Agreement No. DMR-1157490, the State of Florida, and the U.S. DoE. In accordance with the EPSRC policy framework on research data, access to the data will be made available from Ref. 47.

-
- * roger.johnson@physics.ox.ac.uk
- ¹ J. G. Rau, E. K.-H. Lee, and H.-Y. Kee, arXiv:1507.06323 .
 - ² A. Kitaev, *Annals of Physics* **321**, 2 (2006).
 - ³ G. Jackeli and G. Khaliullin, *Phys. Rev. Lett.* **102**, 017205 (2009).
 - ⁴ J. Chaloupka, G. Jackeli, and G. Khaliullin, *Phys. Rev. Lett.* **105**, 027204 (2010).
 - ⁵ A. Biffin, R. D. Johnson, I. Kimchi, R. Morris, A. Bombardi, J. G. Analytis, A. Vishwanath, and R. Coldea, *Phys. Rev. Lett.* **113**, 197201 (2014).
 - ⁶ A. Biffin, R. D. Johnson, S. Choi, F. Freund, S. Manni, A. Bombardi, P. Manuel, P. Gegenwart, and R. Coldea, *Phys. Rev. B* **90**, 205116 (2014).
 - ⁷ I. Kimchi, R. Coldea, and A. Vishwanath, *Phys. Rev. B* **91**, 245134 (2015).
 - ⁸ E. K.-H. Lee and Y. B. Kim, *Phys. Rev. B* **91**, 064407 (2015).
 - ⁹ E. K.-H. Lee, J. G. Rau, and Y. B. Kim, arXiv:1506.06746 .
 - ¹⁰ X. Liu, T. Berlijn, W.-G. Yin, W. Ku, A. Tsvelik, Y.-J. Kim, H. Gretarsson, Y. Singh, P. Gegenwart, and J. P. Hill, *Phys. Rev. B* **83**, 220403 (2011).
 - ¹¹ S. K. Choi, R. Coldea, A. N. Kolmogorov, T. Lancaster, I. I. Mazin, S. J. Blundell, P. G. Radaelli, Y. Singh, P. Gegenwart, K. R. Choi, S.-W. Cheong, P. J. Baker, C. Stock, and J. Taylor, *Phys. Rev. Lett.* **108**, 127204 (2012).
 - ¹² F. Ye, S. Chi, H. Cao, B. C. Chakoumakos, J. A. Fernandez-Baca, R. Custelcean, T. F. Qi, O. B. Korneta, and G. Cao, *Phys. Rev. B* **85**, 180403 (2012).
 - ¹³ J. Chaloupka and G. Khaliullin, *Phys. Rev. B* **92**, 024413 (2015).
 - ¹⁴ S. Hwan Chun, J.-W. Kim, J. Kim, H. Zheng, C. C. Stoumpos, C. D. Malliakas, J. F. Mitchell, K. Mehlawat, Y. Singh, Y. Choi, T. Gog, A. Al-Zein, M. M. Sala, M. Krisch, J. Chaloupka, G. Jackeli, G. Khaliullin, and B. J. Kim, *Nat. Phys.* **11**, 462 (2015).
 - ¹⁵ K. W. Plumb, J. P. Clancy, L. J. Sandilands, V. V. Shankar, Y. F. Hu, K. S. Burch, H.-Y. Kee, and Y.-J. Kim, *Phys. Rev. B* **90**, 041112 (2014).
 - ¹⁶ H.-S. Kim, V. S. V., A. Catuneanu, and H.-Y. Kee, *Phys. Rev. B* **91**, 241110 (2015).
 - ¹⁷ J. A. Sears, M. Songvilay, K. W. Plumb, J. P. Clancy, Y. Qiu, Y. Zhao, D. Parshall, and Y.-J. Kim, *Phys. Rev. B* **91**, 144420 (2015).
 - ¹⁸ A. Banerjee, C. Bridges, J.-Q. Yan, A. Aczel, L. Li, M. Stone, G. Granroth, M. Lumsden, Y. Yiu, J. Knolle, D. Kovrizhin, S. Bhattacharjee, R. Moessner, D. Tennant, D. Mandrus, and S. Nagler, arXiv:1504.08037 .
 - ¹⁹ Y. Kubota, H. Tanaka, T. Ono, Y. Narumi, and K. Kindo, *Phys. Rev. B* **91**, 094422 (2015).
 - ²⁰ M. Majumder, M. Schmidt, H. Rosner, A. A. Tsirlin, H. Yasuoka, and M. Baenitz, *Phys. Rev. B* **91**, 180401 (2015).
 - ²¹ L. J. Sandilands, Y. Tian, H.-S. Reijnders, A. A. and Kim, K. W. Plumb, H.-Y. Kee, Y.-J. Kim, and K. S. Burch, arXiv:1503.07593 .
 - ²² L. J. Sandilands, Y. Tian, K. W. Plumb, Y.-J. Kim, and K. S. Burch, *Phys. Rev. Lett.* **114**, 147201 (2015).
 - ²³ I. Rousochatzakis, J. Reuther, R. Thomale, S. Rachel, and N. B. Perkins, arXiv:1506.09185 .
 - ²⁴ J. M. Fletcher, W. E. Gardner, A. C. Fox, and G. Topping, *J. Chem. Soc. A* , 1038 (1967).
 - ²⁵ Y. Kobayashi, T. Okada, K. Asai, M. Katada, H. Sano, and F. Ambe, *Inorganic Chemistry* **31**, 4570 (1992).
 - ²⁶ K. Brodersen, F. Moers, and H. Schnering, *Naturwissenschaften* **52**, 205 (1965).
 - ²⁷ E. Stroganov and K. Ovchinnikov, *Vestn. Leningrad. Univ., Fizika, Khimiya* **12**, 152 (1957).
 - ²⁸ H. von Schnering, K. Brodersen, F. Moers, H. Breitbach, and G. Thiele, *Journal of the Less Common Metals* **11**, 288 (1966).
 - ²⁹ K. Brodersen, G. Thiele, H. Ohnsorge, I. Recke, and F. Moers, *Journal of the Less Common Metals* **15**, 347 (1968).

- ³⁰ H.-J. Cantow, H. Hillebrecht, S. N. Magonov, H. W. Rotter, M. Drechsler, and G. Thiele, *Angewandte Chemie International Edition in English* **29**, 537 (1990).
- ³¹ J. A. A. Ketelaar, C. H. MacGillavry, and P. A. Renes, *Recl. Trav. Chim. Pays-Bas* **66**, 501 (1947).
- ³² M. J. O'Malley, H. Verweij, and P. M. Woodward, *Journal of Solid State Chemistry* **181**, 1803 (2008).
- ³³ P. A. Goddard, J. Singleton, P. Sengupta, R. D. McDonald, T. Lancaster, S. J. Blundell, F. L. Pratt, S. Cox, N. Harrison, J. L. Manson, H. I. Southerland, and J. A. Schlueter, *New Journal of Physics* **10**, 083025 (2008).
- ³⁴ M. Jaime, A. Lacerda, Y. Takano, and G. S. Boebinger, *Journal of Physics: Conference Series* **51**, 643 (2006).
- ³⁵ P. Blaha, K. Schwarz, G. K. H. Madsen, D. Kvasnicka, J. Luitz. WIEN2k, *An Augmented Plane Wave + Local Orbitals Program for Calculating Crystal Properties*. (Karlheinz Schwarz, Techn. Universität Wien, Austria, 2001).
- ³⁶ K. Koepernik and H. Eschrig, *Phys. Rev. B* **59**, 1743 (1999).
- ³⁷ S. Hendricks and E. Teller, *J. Chem. Phys.* **10**, 147 (1942).
- ³⁸ J. Rodríguez-Carvajal, *Physica B* **192**, 55 (1993).
- ³⁹ G. Kresse and J. Hafner, *Phys. Rev. B* **47**, 558 (1993).
- ⁴⁰ J. P. Perdew, K. Burke, and M. Ernzerhof, *Phys. Rev. Lett.* **77**, 3865 (1996).
- ⁴¹ B. Morosin and A. Narath, *J. Chem. Phys.* **40**, 1958 (1964).
- ⁴² M. Kenzelmann, R. Coldea, D. A. Tennant, D. Visser, M. Hofmann, P. Smeibidl, and Z. Tylczynski, *Phys. Rev. B* **65**, 144432 (2002).
- ⁴³ H.-C. Jiang, Z.-C. Gu, X.-L. Qi, and S. Trebst, *Phys. Rev. B* **83**, 245104 (2011).
- ⁴⁴ I. I. Mazin, H. O. Jeschke, K. Foyevtsova, R. Valentí, and D. I. Khomskii, *Phys. Rev. Lett.* **109**, 197201 (2012).
- ⁴⁵ K. Foyevtsova, H. O. Jeschke, I. I. Mazin, D. I. Khomskii, and R. Valentí, *Phys. Rev. B* **88**, 035107 (2013).
- ⁴⁶ Y. Li, K. Foyevtsova, H. O. Jeschke, and R. Valentí, *Phys. Rev. B* **91**, 161101 (2015).
- ⁴⁷ <http://dx.doi.org/10.5287/bodleian:3f4625467>.